Eur. Phys. J. B **51**, 461–472 (2006)
DOI: 10.1140/epjb/e2006-00258-x

THE EUROPEAN PHYSICAL JOURNAL B

d = 3 anisotropic and d = 2 tJ models: phase diagrams, thermodynamic properties, and chemical potential shift

M. Hinczewski[1,2] and A.N. Berker[1−4,a]

[1] Feza Gürsey Research Institute, TÜBITAK - Bosphorus University, Çengelköy 34680, Istanbul, Turkey
[2] Department of Physics, Massachusetts Institute of Technology, Cambridge, Massachusetts 02139, USA
[3] Department of Physics, Koç University, Sarıyer 34450, Istanbul, Turkey
[4] Department of Physics, Istanbul Technical University, Maslak 34469, Istanbul, Turkey

Received 24 January 2006
Published online 28 June 2006 –

Abstract. The anisotropic $d = 3$ tJ model is studied by renormalization-group theory, yielding the evolution of the system as interplane coupling is varied from the isotropic three-dimensional to quasi-two-dimensional regimes. Finite-temperature phase diagrams, chemical potential shifts, and in-plane and interplane kinetic energies and antiferromagnetic correlations are calculated for the entire range of electron densities. We find that the novel τ phase, seen in earlier studies of the isotropic $d = 3$ tJ model, persists even for strong anisotropy. While the τ phase appears at low temperatures at 30–35% hole doping away from $\langle n_i \rangle = 1$, at smaller hole dopings we see a complex lamellar structure of antiferromagnetic and disordered regions, with a suppressed chemical potential shift, a possible marker of incommensurate ordering in the form of microscopic stripes. An investigation of the renormalization-group flows for the isotropic two-dimensional tJ model also shows a clear pre-signature of the τ phase, which in fact appears with finite transition temperatures upon addition of the smallest interplane coupling.

PACS. 74.72.-h Cuprate superconductors (high-T_c and insulating parent compounds) – 71.10.Fd Lattice fermion models (Hubbard model, etc.) – 05.30.Fk Fermion systems and electron gas – 74.25.Dw Superconductivity phase diagrams

1 Introduction

The anisotropic nature of high-T_c materials, where groups of one or more CuO_2 planes are weakly coupled through block layers that act as charge reservoirs, has led to intense theoretical focus on two-dimensional models of electron conduction [1]. However, a full understanding of the cuprates will require taking into account physics along the third dimension. Crucial aspects of the phase diagram, like the finite value of the Néel temperature, depend on interplanar coupling [2], and going beyond two dimensions is also necessary to explain the behavior of T_c as the number of CuO_2 layers per unit cell is increased [3]. Moreover, given the recent debate over the adequacy of the two-dimensional tJ model as a description of high-T_c superconductivity [4–7], a resolution of the issue might be found by turning to highly anisotropic three-dimensional models [7].

As a simplified description of strongly correlated electrons in an anisotropic system, we look at the tJ model on a cubic lattice with uniform interaction strengths in the xy planes, and a weaker interaction in the z direction. To obtain a finite-temperature phase diagram for the entire range of electron densities, we extend to anisotropic systems the renormalization-group approach that has been applied successfully in earlier studies of both tJ and Hubbard models as isotropic $d = 3$ systems [8–11]. For the $d = 3$ isotropic tJ model, this approach has yielded an interesting phase diagram with antiferromagnetism near $\langle n_i \rangle = 1$ and a new low-temperature "τ" phase for 33–37% hole doping. Within this τ phase, the magnitude of the electron hopping strength in the Hamiltonian tends to infinity as the system is repeatedly rescaled [8]. The calculated superfluid weight shows a marked peak in the τ phase, and both the temperature profile of the superfluid weight and the density of free carriers with hole doping is reminiscent of experimental results in cuprates [11]. Given these apparent links with cuprate physics, the next logical step is to ask whether the τ phase is present in the strongly anisotropic regime, which is the one directly relevant to experiments.

The extension of the position-space renormalization-group method to spatial anisotropy has recently been

[a] e-mail: nberker@ku.edu.tr

demonstrated with $d = 3$ Ising, XY magnetic and percolation systems [12]. We apply a similar anisotropic generalization to the electronic conduction model and find the evolution of the phase diagram from the isotropic $d = 3$ to the quasi $d = 2$ cases. While transition temperatures become lower, the τ phase does continue to exist even for very weak interplanar coupling. The density range of the τ phase remains stable as anisotropy is increased, while for 5–30% hole doping an intricate structure of antiferromagnetic and disordered phases develops, a possible indicator of underlying incommensurate order, manifested through the formation of microscopic stripes. Consistent with this interpretation, our system in this density range shows a characteristic "pinning" of the chemical potential with hole doping.

Lastly, we turn from the $d = 3$ anisotropic case to the $d = 2$ tJ model, where earlier studies [8,9] have found no τ phase (but have elucidated the occurrence/non-occurrence of phase separation). Nevertheless, by looking at the low-temperature behavior of the renormalization-group flows, we find a compelling pre-signature of the τ phase even in $d = 2$, at exactly the density range where the τ phase appears when the slightest interplanar coupling is added to the system.

2 Anisotropic tJ Hamiltonian

We consider the tJ Hamiltonian on a cubic lattice with different interaction strengths for nearest neighbors lying in the xy plane or along the z direction (respectively denoted by $\langle ij\rangle_{xy}$ and $\langle ij\rangle_z$):

$$\begin{aligned} H = P \Bigg[& \tilde{t}_{xy} \sum_{\langle ij\rangle_{xy},\sigma} \left(c^\dagger_{i\sigma} c_{j\sigma} + c^\dagger_{j\sigma} c_{i\sigma} \right) \\ & + \tilde{t}_z \sum_{\langle ij\rangle_z,\sigma} \left(c^\dagger_{i\sigma} c_{j\sigma} + c^\dagger_{j\sigma} c_{i\sigma} \right) \\ & + \tilde{J}_{xy} \sum_{\langle ij\rangle_{xy}} \mathbf{S}_i \cdot \mathbf{S}_j + \tilde{J}_z \sum_{\langle ij\rangle_z} \mathbf{S}_i \cdot \mathbf{S}_j \\ & - \tilde{V}_{xy} \sum_{\langle ij\rangle_{xy}} n_i n_j - \tilde{V}_z \sum_{\langle ij\rangle_z} n_i n_j - \tilde{\mu} \sum_i n_i \Bigg] P \,. \end{aligned} \tag{1}$$

Here $c^\dagger_{i\sigma}$ and $c_{i\sigma}$ are creation and annihilation operators, obeying anticommutation rules, for an electron with spin $\sigma = \uparrow$ or $\downarrow$ at lattice site i, $n_{i\sigma} = c^\dagger_{i\sigma} c_{i\sigma}$, $n_i = n_{i\uparrow} + n_{i\downarrow}$ are the number operators, and $\mathbf{S}_i = \frac{1}{2} \sum_{\sigma\sigma'} c^\dagger_{i\sigma} \mathbf{s}_{\sigma\sigma'} c_{i\sigma'}$ is the single-site spin operator, with $\mathbf{s}$ the vector of Pauli spin matrices. The entire Hamiltonian is sandwiched between projection operators $P = \prod_i (1 - n_{i\downarrow} n_{i\uparrow})$, which project out states with doubly-occupied sites. The standard, isotropic tJ Hamiltonian obtains when $\tilde{t}_{xy} = \tilde{t}_z$, $\tilde{J}_{xy} = \tilde{J}_z$, $\tilde{V}_{xy} = \tilde{V}_z$, and $\tilde{V}_{xy}/\tilde{J}_{xy} = \tilde{V}_z/\tilde{J}_z = 1/4$.

For simplicity, we rewrite equation (1) using dimensionless interaction constants, and rearrange the $\tilde{\mu}$ chemical potential term to group the Hamiltonian into summations over the xy and z bonds:

$$\begin{aligned} -\beta H = & \sum_{\langle ij\rangle_{xy}} P \Bigg[-t_{xy} \sum_\sigma \left(c^\dagger_{i\sigma} c_{j\sigma} + c^\dagger_{j\sigma} c_{i\sigma} \right) \\ & - J_{xy} \mathbf{S}_i \cdot \mathbf{S}_j + V_{xy} n_i n_j + \mu (n_i + n_j) \Bigg] P \\ & + \sum_{\langle ij\rangle_z} P \Bigg[-t_z \sum_\sigma \left(c^\dagger_{i\sigma} c_{j\sigma} + c^\dagger_{j\sigma} c_{i\sigma} \right) \\ & - J_z \mathbf{S}_i \cdot \mathbf{S}_j + V_z n_i n_j + \mu (n_i + n_j) \Bigg] P \\ \equiv & \sum_{\langle ij\rangle_{xy}} \{ -\beta H_{xy}(i,j) \} + \sum_{\langle ij\rangle_z} \{ -\beta H_z(i,j) \} \,. \end{aligned} \tag{2}$$

Here $\beta = 1/k_B T$, so that the interaction constants are related by $t_{xy} = \beta \tilde{t}_{xy}$, $t_z = \beta \tilde{t}_z$, $J_{xy} = \beta \tilde{J}_{xy}$, $J_z = \beta \tilde{J}_z$, $V_{xy} = \beta \tilde{V}_{xy}$, $V_z = \beta \tilde{V}_z$, and $\mu = \beta \tilde{\mu}/6$.

3 Renormalization-group theory

3.1 Isotropic transformation and anisotropic expectations

Since the isotropic model is a special case of equation (1), let us briefly outline the main steps in effecting the renormalization equations of earlier, isotropic studies [8,9,11]. We begin by setting up a decimation transformation for a one-dimensional tJ chain, finding a thermodynamically equivalent Hamiltonian by tracing over the degrees of freedom at every other lattice site. With the vector $\mathbf{K}$ whose elements are the interaction constants in the Hamiltonian, the decimation can be expressed as a mapping of the original $d = 1$ system onto a new system with interaction constants

$$\mathbf{K}' = \mathbf{R}(\mathbf{K}) \,. \tag{3}$$

The Migdal-Kadanoff [13,14] procedure has been remarkably successful, for systems both classical and quantum, in extending this transformation to $d > 1$ (for an overview, see [10]). In this procedure, a subset of the nearest-neighbor interactions in the lattice are ignored, leaving behind a new d-dimensional hypercubic lattice where each point is connected to its neighbor by two consecutive nearest-neighbor segments of the original lattice. The decimation described above is applied to the middle site between the two consecutive segments, giving the renormalized nearest-neighbor couplings for the points forming the new lattice. We compensate for the interactions that are ignored in the original lattice by multiplying the interactions after the decimation by b^{d-1}, where $b = 2$ is the length rescaling factor. Thus for $d > 1$ the renormalization-group transformation of equation (3) generalizes to

$$\mathbf{K}' = b^{d-1} \mathbf{R}(\mathbf{K}), \tag{4}$$

which, through flows in a four-dimensional Hamiltonian space (for the Hubbard model, 10-dimensional

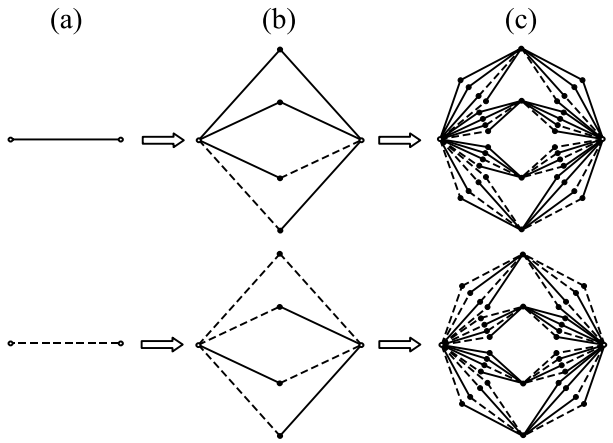

Fig. 1. Construction of the hierarchical model in Section 2.2. Solid lines correspond to xy bonds, while dashed lines correspond to z bonds.

Hamiltonian space [10]), yields a rich array of physical phenomena.

With the anisotropic tJ Hamiltonian on a cubic lattice (Eq. (1)), there are two intercoupled sets of interaction constants, $\mathbf{K}_{xy}$ and $\mathbf{K}_z$, and further development of the transformation is needed. However, there are three particular instances where the transformation in equation (4) is directly applicable. When $\mathbf{K}_{xy} = \mathbf{K}_z$, we have the $d = 3$ isotropic case, so the appropriate renormalization-group equations are

$$\mathbf{K}'_{xy} = 4\,\mathbf{R}(\mathbf{K}_{xy})\,, \qquad \mathbf{K}'_z = 4\,\mathbf{R}(\mathbf{K}_z)\,. \tag{5}$$

When $\mathbf{K}_{xy} \neq 0$ and $\mathbf{K}_z = 0$, we have a system of decoupled isotropic $d = 2$ planes, and the transformation is given by

$$\mathbf{K}'_{xy} = 2\,\mathbf{R}(\mathbf{K}_{xy})\,, \qquad \mathbf{K}'_z = 0\,. \tag{6}$$

Similarly, when $\mathbf{K}_{xy} = 0$ and $\mathbf{K}_z \neq 0$, we have decoupled $d = 1$ chains, and

$$\mathbf{K}'_{xy} = 0\,, \qquad \mathbf{K}'_z = \mathbf{R}(\mathbf{K}_z)\,. \tag{7}$$

The renormalization-group transformation for the anisotropic model described in the following sections recovers the correct results, equations (5)–(7), for these three cases.

3.2 Hierarchical lattice model for anisotropy

A one-to-one correspondence exists between Migdal-Kadanoff and other approximate renormalization-group transformations on the one hand, and exact renormalization-group transformations of corresponding hierarchical lattices on the other hand, through the sharing of identical recursion relations [15–17]. The correspondence guarantees the fulfillment of general physical preconditions on the results of approximate renormalization-group transformations, since the latter are thus "physically realizable" [15]. This correspondence has recently been exploited to develop renormalization-group transformations for spatially anisotropic Ising, XY magnetic and percolation systems [12]. Similarly, to derive an approximate renormalization-group transformation for the anisotropic tJ Hamiltonian, consider the nonuniform hierarchical model depicted in Figure 1. The two types of bonds in the lattice, corresponding to xy and z bonds, are drawn with solid and dashed lines respectively. The hierarchical model is constructed by replacing each single bond of a given type with the connected cluster of bonds shown in Figure 1b, and repeating this step an arbitrary number of times. Figure 1c shows the next stage in the construction for the two graphs in column (b). The renormalization-group transformation on this hierarchical lattice consists of decimating over the four inner sites in each cluster, to generate a renormalized interaction between the two outer sites, thus reversing the construction process, going from the graphs in column (b) of Figure 1 to those in column (a). This renormalization-group transformation has the desired feature that in all three of the cases described above, it reproduces the various isotropic recursion relations of equations (5)–(7).

3.3 Renormalization-group equations for anisotropic system

The hierarchical lattice can be subdivided into individual clusters of bonds shown in Figure 1b. We label these two types of clusters the "xy cluster" (Fig. 1b top) and the "z cluster" (Fig. 1b bottom). The sum over $\langle ij\rangle_{xy\ \mathrm{clus}}$ denotes a sum over the outer sites of all the xy clusters, and analogously $\langle ij\rangle_{z\ \mathrm{clus}}$ denotes a sum over the outer sites of all z clusters. For a given cluster with outer sites ij, the associated inner sites are labeled $k_1^{(ij)}, \ldots, k_4^{(ij)}$. Then the tJ Hamiltonian on the anisotropic lattice has the form

$$\begin{aligned}
-\beta H = \sum_{\langle ij\rangle_{xy\ \mathrm{clus}}} \Big[& -\beta H_{xy}(i, k_1^{(ij)}) - \beta H_{xy}(k_1^{(ij)}, j) \\
& - \beta H_{xy}(i, k_2^{(ij)}) - \beta H_{xy}(k_2^{(ij)}, j) \\
& - \beta H_{xy}(i, k_3^{(ij)}) - \beta H_z(k_3^{(ij)}, j) \\
& - \beta H_z(i, k_4^{(ij)}) - \beta H_{xy}(k_4^{(ij)}, j) \Big] \\
+ \sum_{\langle ij\rangle_{z\ \mathrm{clus}}} \Big[& -\beta H_z(i, k_1^{(ij)}) - \beta H_z(k_1^{(ij)}, j) \\
& - \beta H_z(i, k_2^{(ij)}) - \beta H_{xy}(k_2^{(ij)}, j) \\
& - \beta H_{xy}(i, k_3^{(ij)}) - \beta H_z(k_3^{(ij)}, j) - \beta H_z(i, k_4^{(ij)}) \\
& - \beta H_{xy}(k_4^{(ij)}, j) \Big]\,.
\end{aligned} \tag{8}$$

The renormalization-group transformation consists of finding a thermodynamically equivalent Hamiltonian $-\beta' H'$ that involves only the outer sites of each cluster. Since we are dealing with a quantum system, the non-commutation of the operators in the Hamiltonian means that this decimation, tracing over the degrees of

$$
\begin{aligned}
\mathrm{Tr}_{k\ \mathrm{sites}}\, e^{-\beta H} \simeq & \prod_{\langle ij\rangle_{xy}\ \mathrm{clus}} \Big[\mathrm{Tr}_{k_1^{(ij)}}\, e^{-\beta H_{xy}(i,k_1^{(ij)})-\beta H_{xy}(k_1^{(ij)},j)}\, \mathrm{Tr}_{k_2^{(ij)}}\, e^{-\beta H_{xy}(i,k_2^{(ij)})-\beta H_{xy}(k_2^{(ij)},j)} \\
& \qquad \mathrm{Tr}_{k_3^{(ij)}}\, e^{-\beta H_{xy}(i,k_3^{(ij)})-\beta H_z(k_3^{(ij)},j)}\, \mathrm{Tr}_{k_4^{(ij)}}\, e^{-\beta H_z(i,k_4^{(ij)})-\beta H_{xy}(k_4^{(ij)},j)} \Big] \\
& \times \prod_{\langle ij\rangle_{z}\ \mathrm{clus}} \Big[\mathrm{Tr}_{k_1^{(ij)}}\, e^{-\beta H_z(i,k_1^{(ij)})-\beta H_z(k_1^{(ij)},j)}\, \mathrm{Tr}_{k_2^{(ij)}}\, e^{-\beta H_z(i,k_2^{(ij)})-\beta H_{xy}(k_2^{(ij)},j)} \\
& \qquad \mathrm{Tr}_{k_3^{(ij)}}\, e^{-\beta H_{xy}(i,k_3^{(ij)})-\beta H_z(k_3^{(ij)},j)}\, \mathrm{Tr}_{k_4^{(ij)}}\, e^{-\beta H_z(i,k_4^{(ij)})-\beta H_{xy}(k_4^{(ij)},j)} \Big] \\
= & \prod_{\langle ij\rangle_{xy}\ \mathrm{clus}} \Big[e^{-\beta' H'_{xy,xy}(i,j)} e^{-\beta' H'_{xy,xy}(i,j)} e^{-\beta' H'_{xy,z}(i,j)} e^{-\beta' H'_{z,xy}(i,j)} \Big] \\
& \times \prod_{\langle ij\rangle_{z}\ \mathrm{clus}} \Big[e^{-\beta' H'_{z,z}(i,j)} e^{-\beta' H'_{xy,z}(i,j)} e^{-\beta' H'_{z,xy}(i,j)} e^{-\beta' H'_{z,xy}(i,j)} \Big] \\
\simeq & \, e^{\sum_{\langle ij\rangle_{xy}\ \mathrm{clus}} \left[-2\beta' H'_{xy,xy}(i,j)-\beta' H'_{xy,z}(i,j)-\beta' H'_{z,xy}(i,j)\right] + \sum_{\langle ij\rangle_{z}\ \mathrm{clus}} \left[-\beta' H'_{z,z}(i,j)-\beta' H'_{xy,z}(i,j)-2\beta' H'_{z,xy}(i,j)\right]} \\
= & \, e^{\sum_{\langle ij\rangle_{xy}\ \mathrm{clus}} \left[-\beta' H'_{xy}(i,j)\right] + \sum_{\langle ij\rangle_{z}\ \mathrm{clus}} \left[-\beta' H'_{z}(i,j)\right]} = e^{-\beta' H'} \,. \qquad (9)
\end{aligned}
$$

freedom at the k sites, can only be carried out approximately [18,19]:

see equation (9) above

Here $-\beta' H'_{A,B}(i,j)$, where A, B can each be either xy or z, is

$$e^{-\beta' H'_{A,B}(i,j)} = \mathrm{Tr}_k\, e^{-\beta H_A(i,k)-\beta H_B(k,j)} \,. \qquad (10)$$

In the two approximate steps, marked by $\simeq$ in equation (9), we ignore the non-commutation of operators outside three-site segments of the unrenormalized system. (On the other hand, anticommutation rules are correctly accounted for within the three-site segments, at all successive length scales in the iterations of the renormalization-group transformation.) These two steps involve the same approximation but in opposite directions, which gives some mutual compensation. This approach has been shown to successfully predict finite-temperature behavior in earlier studies [18,19].

Derivation of the renormalization-group equations involves extracting the algebraic form of the operators $-\beta' H'_{A,B}(i,j)$ from equation (10). Since $e^{-\beta' H'_{A,B}(i,j)}$ and $e^{-\beta H_A(i,k)-\beta H_B(k,j)}$ act on the space of two-site and three-site states respectively, equation (10) can be rewritten in terms of matrix elements as

$$
\begin{aligned}
&\langle u_i v_j | e^{-\beta' H'_{A,B}(i,j)} | \bar{u}_i \bar{v}_j \rangle = \\
&\qquad \sum_{w_k} \langle u_i w_k v_j | e^{-\beta H_A(i,k)-\beta H_B(k,j)} | \bar{u}_i w_k \bar{v}_j \rangle \,, \qquad (11)
\end{aligned}
$$

where $u_i, w_k, v_j, \bar{u}_i, \bar{v}_j$ are single-site state variables. Equation (11) is the contraction of a 27×27 matrix on the right into a 9×9 matrix on the left. We block-diagonalize the left and right sides of equation (11) by choosing basis states which are the eigenstates of total particle number, total spin magnitude, total spin z-component, and parity. We denote the set of 9 two-site eigenstates by $\{|\phi_p\rangle\}$ and the set of 27 three-site eigenstates by $\{|\psi_q\rangle\}$, and list them in Tables 1 and 2. Equation (11) is rewritten as

$$
\begin{aligned}
&\langle \phi_p | e^{-\beta' H'_{A,B}(i,j)} | \phi_{\bar{p}} \rangle = \\
&\sum_{\substack{u,v,\bar{u},\\ \bar{v},w}} \sum_{q,\bar{q}} \langle \phi_p | u_i v_j \rangle \langle u_i w_k v_j | \psi_q \rangle \\
&\qquad \cdot \langle \psi_q | e^{-\beta H_A(i,k)-\beta H_B(k,j)} | \psi_{\bar{q}} \rangle \langle \psi_{\bar{q}} | \bar{u}_i w_k \bar{v}_j \rangle \langle \bar{u}_i \bar{v}_j | \phi_{\bar{p}} \rangle \,. \qquad (12)
\end{aligned}
$$

Equation (12) yields six independent elements for the matrix $\langle \phi_p | e^{-\beta' H'_{A,B}(i,j)} | \phi_{\bar{p}} \rangle$, labeled γ_p as follows:

$$
\begin{aligned}
&\gamma_p \equiv \langle \phi_p | e^{-\beta' H'_{A,B}(i,j)} | \phi_p \rangle \quad \text{for } p = 1,2,4,6,7, \\
&\gamma_0 \equiv \langle \phi_2 | e^{-\beta' H'_{A,B}(i,j)} | \phi_4 \rangle \,. \qquad (13)
\end{aligned}
$$

The number of γ_p is also the number of interaction strengths that are independently fixed in the Hamiltonian $-\beta' H'_{A,B}(i,j)$, which consequently must have a more general form than the two-site Hamiltonians in equation (2). The generalized form of the pair Hamiltonian is

$$
\begin{aligned}
-\beta H(i,j) = P \Big[& -t \sum_{\sigma} \left(c^{\dagger}_{i\sigma} c_{j\sigma} + c^{\dagger}_{j\sigma} c_{i\sigma} \right) \\
& - J \mathbf{S}_i \cdot \mathbf{S}_j + V n_i n_j \\
& + \mu(n_i + n_j) + \nu(n_i - n_j) + G \Big] P. \qquad (14)
\end{aligned}
$$

The new terms here are: G, the additive constant that appears in all renormalization-group calculations, does not affect the flows, but enters the determination of expectation values; and $\nu(n_i - n_j)$, a staggered term arising from decimation across two consecutive bonds of different strengths. Provisions for handling the ν term will be described later in this section.

To calculate the γ_p, we determine the matrix elements of $-\beta H_A(i,k) - \beta H_B(k,j)$ in the three-site basis $\{\psi_q\}$. $-\beta H_A$ and $-\beta H_B$ have the form of equation (14),

Table 1. The two-site basis states, with the corresponding particle number (n), parity (p), total spin (s), and total spin z-component (m_s) quantum numbers. The states $|\phi_3\rangle$, $|\phi_5\rangle$, and $|\phi_8\rangle$ are obtained by spin reversal from $|\phi_2\rangle$, $|\phi_4\rangle$, and $|\phi_7\rangle$, respectively.

n	p	s	m_s	Two-site basis states
0	+	0	0	$\|\phi_1\rangle = \|\circ\,\circ\rangle$
1	+	1/2	1/2	$\|\phi_2\rangle = \frac{1}{\sqrt{2}}\{\|\uparrow\,\circ\rangle + \|\circ\,\uparrow\rangle\}$
1	−	1/2	1/2	$\|\phi_4\rangle = \frac{1}{\sqrt{2}}\{\|\uparrow\,\circ\rangle - \|\circ\,\uparrow\rangle\}$
2	−	0	0	$\|\phi_6\rangle = \frac{1}{\sqrt{2}}\{\|\uparrow\downarrow\rangle - \|\downarrow\uparrow\rangle\}$
2	+	1	1	$\|\phi_7\rangle = \|\uparrow\uparrow\rangle$
2	+	1	0	$\|\phi_9\rangle = \frac{1}{\sqrt{2}}\{\|\uparrow\downarrow\rangle + \|\downarrow\uparrow\rangle\}$

Table 2. The three-site basis states, with the corresponding particle number (n), parity (p), total spin (s), and total spin z-component (m_s) quantum numbers. The states $|\psi_{4-5}\rangle$, $|\psi_7\rangle$, $|\psi_{15-16}\rangle$, $|\psi_{19}\rangle$, $|\psi_{21}\rangle$, $|\psi_{23}\rangle$, $|\psi_{26-27}\rangle$ are obtained by spin reversal from $|\psi_{2-3}\rangle$, $|\psi_6\rangle$, $|\psi_{11-12}\rangle$, $|\psi_{17}\rangle$, $|\psi_{20}\rangle$, $|\psi_{22}\rangle$, $|\psi_{24-25}\rangle$, respectively.

n	p	s	m_s	Three-site basis states
0	+	0	0	$\|\psi_1\rangle = \|\circ\,\circ\,\circ\rangle$
1	+	1/2	1/2	$\|\psi_2\rangle = \|\circ\uparrow\circ\rangle$, $\|\psi_3\rangle = \frac{1}{\sqrt{2}}\{\|\uparrow\,\circ\,\circ\rangle + \|\circ\,\circ\,\uparrow\rangle\}$
1	−	1/2	1/2	$\|\psi_6\rangle = \frac{1}{\sqrt{2}}\{\|\uparrow\,\circ\,\circ\rangle - \|\circ\,\circ\,\uparrow\rangle\}$
2	+	0	0	$\|\psi_8\rangle = \frac{1}{2}\{\|\uparrow\downarrow\,\circ\rangle - \|\downarrow\uparrow\,\circ\rangle - \|\circ\uparrow\downarrow\rangle + \|\circ\downarrow\uparrow\rangle\}$
2	−	0	0	$\|\psi_9\rangle = \frac{1}{2}\{\|\uparrow\downarrow\,\circ\rangle - \|\downarrow\uparrow\,\circ\rangle + \|\circ\uparrow\downarrow\rangle - \|\circ\downarrow\uparrow\rangle\}$, $\|\psi_{10}\rangle = \frac{1}{\sqrt{2}}\{\|\uparrow\circ\downarrow\rangle - \|\downarrow\circ\uparrow\rangle\}$
2	+	1	1	$\|\psi_{11}\rangle = \|\uparrow\circ\uparrow\rangle$, $\|\psi_{12}\rangle = \frac{1}{\sqrt{2}}\{\|\uparrow\uparrow\,\circ\rangle + \|\circ\uparrow\uparrow\rangle\}$
2	+	1	0	$\|\psi_{13}\rangle = \frac{1}{2}\{\|\uparrow\downarrow\,\circ\rangle + \|\downarrow\uparrow\,\circ\rangle + \|\circ\uparrow\downarrow\rangle + \|\circ\downarrow\uparrow\rangle\}$, $\|\psi_{14}\rangle = \frac{1}{\sqrt{2}}\{\|\uparrow\circ\downarrow\rangle + \|\downarrow\circ\uparrow\rangle\}$
2	−	1	1	$\|\psi_{17}\rangle = \frac{1}{\sqrt{2}}\{\|\uparrow\uparrow\,\circ\rangle - \|\circ\uparrow\uparrow\rangle\}$
2	−	1	0	$\|\psi_{18}\rangle = \frac{1}{2}\{\|\uparrow\downarrow\,\circ\rangle + \|\downarrow\uparrow\,\circ\rangle - \|\circ\uparrow\downarrow\rangle - \|\circ\downarrow\uparrow\rangle\}$
3	+	1/2	1/2	$\|\psi_{20}\rangle = \frac{1}{\sqrt{6}}\{2\|\uparrow\downarrow\uparrow\rangle - \|\uparrow\uparrow\downarrow\rangle - \|\downarrow\uparrow\uparrow\rangle\}$
3	−	1/2	1/2	$\|\psi_{22}\rangle = \frac{1}{\sqrt{2}}\{\|\uparrow\uparrow\downarrow\rangle - \|\downarrow\uparrow\uparrow\rangle\}$
3	+	3/2	3/2	$\|\psi_{24}\rangle = \|\uparrow\uparrow\uparrow\rangle$
3	+	3/2	1/2	$\|\psi_{25}\rangle = \frac{1}{\sqrt{3}}\{\|\uparrow\downarrow\uparrow\rangle + \|\uparrow\uparrow\downarrow\rangle + \|\downarrow\uparrow\uparrow\rangle\}$

with interaction constants $\{t_A, J_A, V_A, \mu_A, \nu_A, G_A\}$ and $\{t_B, J_B, V_B, \mu_B, \nu_B, G_B\}$ respectively. The resulting matrix elements are listed in Table 3. We exponentiate the matrix blocks to find the elements $\langle\psi_q|e^{-\beta H_A(i,k)-\beta H_B(k,j)}|\psi_{\bar{q}}\rangle$ which enter on the right-hand side of equation (12). In this way the γ_p are obtained as functions of the interaction constants in the unrenormalized two-site Hamiltonians, $\gamma_p = \gamma_p(\{t_A, J_A, \ldots\}, \{t_B, J_B, \ldots\})$.

The matrix elements of $-\beta' H'_{A,B}(i,j)$ in the $\{\phi_p\}$ basis are shown in Table 4. Exponentiating this matrix, we solve

Table 3. Diagonal matrix blocks of the unrenormalized three-site Hamiltonian $-\beta H_A(i,k) - \beta H_B(k,j)$. The Hamiltonian being invariant under spin-reversal, the spin-flipped matrix elements are not shown. The additive constant contribution $G_A + G_B$, occurring at the diagonal terms, is also not shown.

	ψ_1
ψ_1	0

	ψ_2	ψ_3	ψ_6
ψ_2	$\mu_A+\mu_B-\nu_A+\nu_B$	$-\frac{1}{\sqrt{2}}(t_A+t_B)$	$\frac{1}{\sqrt{2}}(t_B-t_A)$
ψ_3	$-\frac{1}{\sqrt{2}}(t_A+t_B)$	$\frac{1}{2}(\mu_A+\mu_B+\nu_A-\nu_B)$	$\frac{1}{2}(\mu_A-\mu_B+\nu_A+\nu_B)$
ψ_6	$\frac{1}{\sqrt{2}}(t_B-t_A)$	$\frac{1}{2}(\mu_A-\mu_B+\nu_A+\nu_B)$	$\frac{1}{2}(\mu_A+\mu_B+\nu_A-\nu_B)$

	ψ_8	ψ_9	ψ_{10}
ψ_8	$\frac{1}{2}(\frac{3}{4}J_A+\frac{3}{4}J_B+V_A+V_B+3\mu_A+3\mu_B-\nu_A+\nu_B)$	$\frac{1}{2}(\frac{3}{4}J_A-\frac{3}{4}J_B+V_A-V_B+\mu_A-\mu_B+\nu_A+\nu_B)$	$\frac{1}{\sqrt{2}}(t_A-t_B)$
ψ_9	$\frac{1}{2}(\frac{3}{4}J_A-\frac{3}{4}J_B+V_A-V_B+\mu_A-\mu_B+\nu_A+\nu_B)$	$\frac{1}{2}(\frac{3}{4}J_A+\frac{3}{4}J_B+V_A+V_B+3\mu_A+3\mu_B-\nu_A+\nu_B)$	$-\frac{1}{\sqrt{2}}(t_A+t_B)$
ψ_{10}	$\frac{1}{\sqrt{2}}(t_A-t_B)$	$-\frac{1}{\sqrt{2}}(t_A+t_B)$	$\mu_A+\mu_B+\nu_A-\nu_B$

	ψ_{11}	ψ_{12}	ψ_{17}
ψ_{11}	$\mu_A+\mu_B+\nu_A-\nu_B$	$-\frac{1}{\sqrt{2}}(t_A+t_B)$	$\frac{1}{\sqrt{2}}(t_A-t_B)$
ψ_{12}	$-\frac{1}{\sqrt{2}}(t_A+t_B)$	$\frac{1}{2}(-\frac{1}{4}J_A-\frac{1}{4}J_B+V_A+V_B+3\mu_A+3\mu_B-\nu_A+\nu_B)$	$\frac{1}{2}(-\frac{1}{4}J_A+\frac{1}{4}J_B+V_A-V_B+\mu_A-\mu_B+\nu_A+\nu_B)$
ψ_{17}	$\frac{1}{\sqrt{2}}(t_A-t_B)$	$\frac{1}{2}(-\frac{1}{4}J_A+\frac{1}{4}J_B+V_A-V_B+\mu_A-\mu_B+\nu_A+\nu_B)$	$\frac{1}{2}(-\frac{1}{4}J_A-\frac{1}{4}J_B+V_A+V_B+3\mu_A+3\mu_B-\nu_A+\nu_B)$

	ψ_{13}	ψ_{14}	ψ_{18}
ψ_{13}	$\frac{1}{2}(-\frac{1}{4}J_A-\frac{1}{4}J_B+V_A+V_B+3\mu_A+3\mu_B-\nu_A+\nu_B)$	$-\frac{1}{\sqrt{2}}(t_A+t_B)$	$\frac{1}{2}(-\frac{1}{4}J_A+\frac{1}{4}J_B+V_A-V_B+\mu_A-\mu_B+\nu_A+\nu_B)$
ψ_{14}	$-\frac{1}{\sqrt{2}}(t_A+t_B)$	$\mu_A+\mu_B+\nu_A-\nu_B$	$\frac{1}{\sqrt{2}}(t_A-t_B)$
ψ_{18}	$\frac{1}{2}(-\frac{1}{4}J_A+\frac{1}{4}J_B+V_A-V_B+\mu_A-\mu_B+\nu_A+\nu_B)$	$\frac{1}{\sqrt{2}}(t_A-t_B)$	$\frac{1}{2}(-\frac{1}{4}J_A-\frac{1}{4}J_B+V_A+V_B+3\mu_A+3\mu_B-\nu_A+\nu_B)$

	ψ_{20}	ψ_{22}
ψ_{20}	$\frac{1}{2}J_A+\frac{1}{2}J_B+V_A+V_B+2\mu_A+2\mu_B$	$\frac{\sqrt{3}}{4}(J_B-J_A)$
ψ_{22}	$\frac{\sqrt{3}}{4}(J_B-J_A)$	$V_A+V_B+2\mu_A+2\mu_B$

	ψ_{24}
ψ_{24}	$-\frac{1}{4}J_A-\frac{1}{4}J_B+V_A+V_B+2\mu_A+2\mu_B$

	ψ_{25}
ψ_{25}	$-\frac{1}{4}J_A-\frac{1}{4}J_B+V_A+V_B+2\mu_A+2\mu_B$

for the renormalized interaction constants (t', J', V', μ', ν', G') in terms of the γ_p:

$$t' = u, \qquad J' = \ln\frac{\gamma_6}{\gamma_7},$$
$$V' = \frac{1}{4}\left\{\ln(\gamma_1^4\gamma_6\gamma_7^3) - 8v\right\}, \qquad \mu' = v - \ln\gamma_1,$$
$$\nu' = \frac{2u\gamma_0}{\gamma_4-\gamma_2}, \qquad G' = \ln\gamma_1, \tag{15}$$

where

$$v = \frac{1}{2}\ln\left(\gamma_2\gamma_4 - \gamma_0^2\right),$$
$$u = \frac{\gamma_4-\gamma_2}{\sqrt{(\gamma_4-\gamma_2)^2+4\gamma_0^2}}\cosh^{-1}\left(\frac{\gamma_4+\gamma_2}{2e^v}\right).$$

Table 4. Block-diagonal matrix of the renormalized two-site Hamiltonian $-\beta' H'(i,j)$. The Hamiltonian being invariant under spin-reversal, the spin-flipped matrix elements are not shown.

	ϕ_1	ϕ_2	ϕ_4	ϕ_6	ϕ_7	ϕ_9
ϕ_1	G					
ϕ_2		$-t' + \mu' + G'$	ν'		0	
ϕ_4		ν'	$t' + \mu' + G'$			
ϕ_6				$\frac{3}{4}J' + V' + 2\mu' + G'$		
ϕ_7			0		$-\frac{1}{4}J' + V' + 2\mu' + G'$	
ϕ_9						$-\frac{1}{4}J' + V' + 2\mu' + G'$

The renormalization-group transformation described by equations (12)–(15) can be expressed as a mapping of a three-site Hamiltonian with bonds having interaction constants $\mathbf{K}_A = \{t_A, J_A, V_A, \mu_A, \nu_A, G_A\}$ and $\mathbf{K}_B = \{t_B, J_B, V_B, \mu_B, \nu_B, G_B\}$ onto a two-site Hamiltonian with interaction constants

$$\mathbf{K}' = \mathbf{R}(\mathbf{K}_A, \mathbf{K}_B)\,. \tag{16}$$

When $\nu_A = \nu_B = 0$, this mapping has the property that if $\mathbf{R}(\mathbf{K}_A, \mathbf{K}_B) = \{t', J', V', \mu', \nu', G'\}$, then $\mathbf{R}(\mathbf{K}_B, \mathbf{K}_A)$ gives the same result, except that the sign of ν' is switched. So $\mathbf{R}(\mathbf{K}_A, \mathbf{K}_A)$ has a zero ν' component when $\nu_A = 0$.

From equation (9), the renormalized xy- and z-bond interaction constants are

$$\begin{aligned}\mathbf{K}'_{xy} &= 2\mathbf{R}(\mathbf{K}_{xy}, \mathbf{K}_{xy}) + \mathbf{R}(\mathbf{K}_{xy}, \mathbf{K}_z) + \mathbf{R}(\mathbf{K}_z, \mathbf{K}_{xy})\,,\\ \mathbf{K}'_z &= \mathbf{R}(\mathbf{K}_z, \mathbf{K}_z) + \mathbf{R}(\mathbf{K}_{xy}, \mathbf{K}_z) + 2\mathbf{R}(\mathbf{K}_z, \mathbf{K}_{xy})\,.\end{aligned} \tag{17}$$

The staggered ν' term cancels out in $\mathbf{K}'_{xy}$. In constructing the anisotropic hierarchical lattice, we could have used a graph in which the lowest two bonds in Figure 1b are interchanged. Averaging over these two realizations,

$$\mathbf{K}'_z = \mathbf{R}(\mathbf{K}_z, \mathbf{K}_z) + \frac{3}{2}\mathbf{R}(\mathbf{K}_{xy}, \mathbf{K}_z) + \frac{3}{2}\mathbf{R}(\mathbf{K}_z, \mathbf{K}_{xy})\,, \tag{18}$$

the ν' term cancels out in $\mathbf{K}'_z$ as well.

4 Phase diagrams and expectation values as a function of anisotropy

Thermodynamic properties of the system, including the global phase diagram and expectation values of operators occurring in the Hamiltonian, are obtained from the analysis of the renormalization-group flows [20]. The initial conditions for the flows are the interaction constants in the original anisotropic tJ Hamiltonian. For the numerical results presented below, we use the following initial form: $t_{xy} = t$, $t_z = \alpha_t t$, $J_{xy} = J$, $J_z = \alpha_J J$, $V_{xy} = J_{xy}/4$, $V_z = J_z/4$, where $0 \le \alpha_t, \alpha_J \le 1$. For the anisotropy parameters α_t and α_J, we use $\alpha_J = \alpha_t^2$, as dictated from the derivation of the tJ Hamiltonian from the large-U limit of the Hubbard model [21].

Table 5. Expectation values at the phase-sink fixed points.

Phase sink	Expectation values			
	$-\sum_\sigma \langle c^\dagger_{i\sigma} c_{j\sigma} + c^\dagger_{j\sigma} c_{i\sigma}\rangle$	$\langle n_i\rangle$	$\langle \mathbf{S}_i \cdot \mathbf{S}_j\rangle$	$\langle n_i n_j\rangle$
d	0	0	0	0
D	0	1	0	1
A	0	1	$\frac{1}{4}$	1
τ	$\frac{2}{3}$	$\frac{2}{3}$	$-\frac{1}{4}$	$\frac{1}{3}$

Phase diagrams for the coupling $J/t = 0.444$ and various values of $\alpha_t = t_z/t_{xy}$ are shown in Figures 2 and 3. The temperature variable is $1/t$, and the diagrams are plotted both in terms of chemical potential μ/J and electron density $\langle n_i\rangle$. The phases in the diagrams are those found in earlier studies of the isotropic $d = 3$ tJ model [8,9], which can be consulted for a more detailed description. Here we summarize the salient features of the phases.

Each phase is associated with a completely stable fixed point (sink) of the renormalization-group flows, and thermodynamic densities calculated at the fixed point epitomize (and determine [11], e.g., as seen in the results displayed in Fig. 4) characteristics of the entire phase. The results are shown in Table 5. The *dilute disordered (d)* and *dense disordered (D)* phases have $\langle n_i\rangle = 0$ and 1 at their respective phase sinks, so the electron densities in these phases are accordingly small in the one case and close to 1 in the other. Both phases lack long-range spin order, since $\langle \mathbf{S}_i \cdot \mathbf{S}_j\rangle = 0$ at the sinks. On the other hand, the *antiferromagnetic (A)* phase has $\langle n_i\rangle = 1$ and a nonzero nearest-neighbor spin-spin correlation $\langle \mathbf{S}_i \cdot \mathbf{S}_j\rangle = 1/4$ at the phase sink. Since nearest-neighbor spins at the sink are distant members of the same sublattice in the unrenormalized system, this positive value for $\langle \mathbf{S}_i \cdot \mathbf{S}_j\rangle$ is expected, and leads to $\langle \mathbf{S}_i \cdot \mathbf{S}_j\rangle < 0$ for nearest neighbors of the original system, as seen in the last row of Figure 4.

In the antiferromagnetic and the two disordered phases, the electron hopping strengths t_{xy} and t_z tend to zero after repeated rescalings. The system is either completely empty or filled in this limit, and the expectation value of the kinetic energy operator $\langle K\rangle \equiv -\sum_\sigma \langle c^\dagger_{i\sigma} c_{j\sigma} + c^\dagger_{j\sigma} c_{i\sigma}\rangle$ is zero at the sink. The τ *phase* is interesting in contrast because the magnitudes of t_{xy} and t_z both tend to ∞, and we find partial filling, $\langle n_i\rangle = 2/3$, and a nonzero kinetic energy $\langle K\rangle = 2/3$ at the phase sink. It should be recalled that we have shown in a previous work [11] that the superfluid weight has a pronounced peak in the τ phase, there is evidence of a gap in the quasiparticle spectrum, and the free carrier density in the vicinity of the τ phase has properties seen experimentally in cuprates [22,23].

Figures 2 and 3 clearly demonstrate that the τ phase is not unique to the isotropic $d = 3$ case, but exists at all values of t_z/t_{xy}, even persisting in the weak interplane coupling limit. Figure 2 shows the evolution of the phase diagram in the strongly anisotropic regime, for t_z/t_{xy}

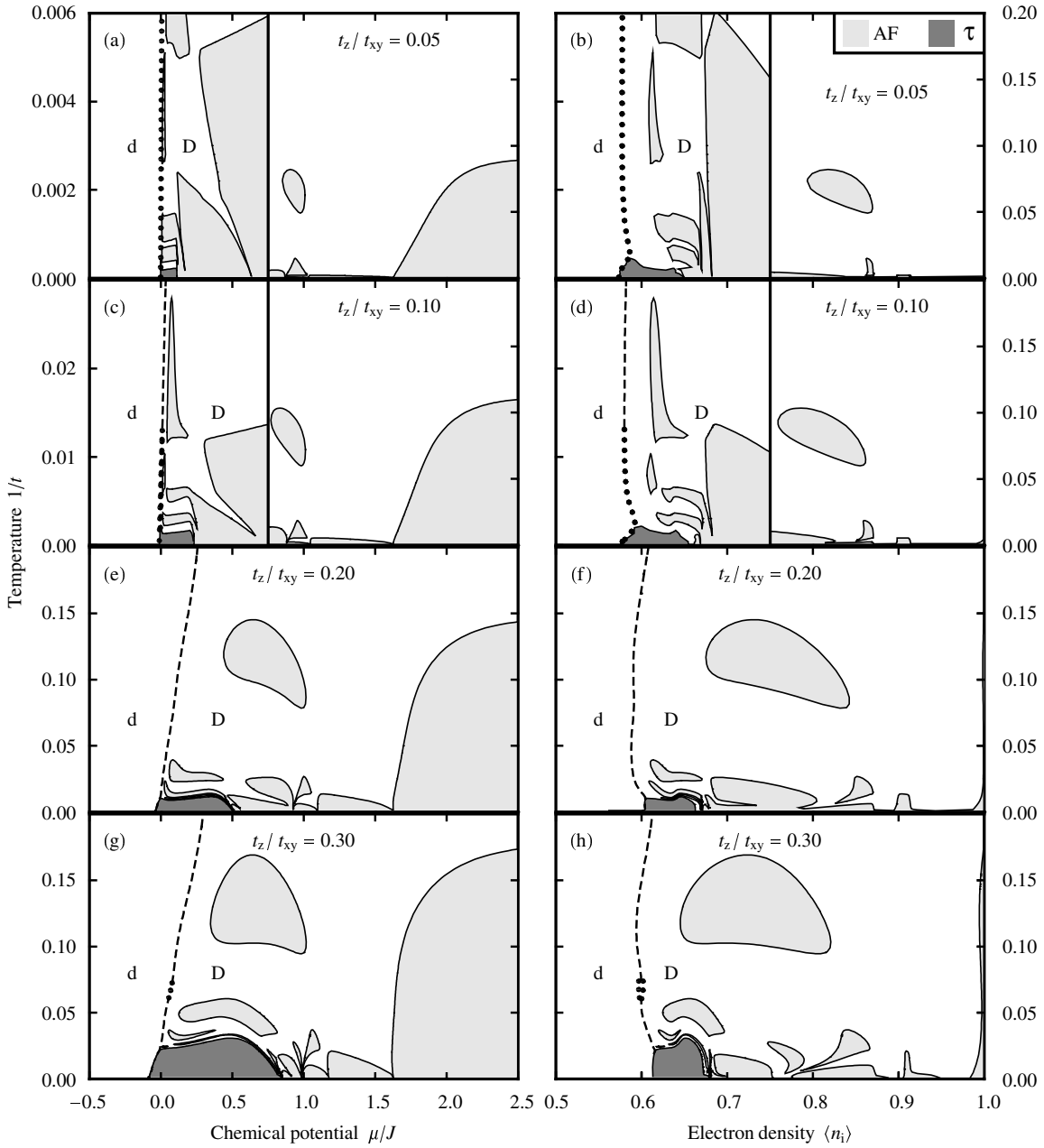

Fig. 2. Phase diagrams of the anisotropic tJ model with $J/t = 0.444$ in temperature vs. chemical potential (first column) and temperature vs. electron density (second column). The degree of anisotropy varies from $t_z/t_{xy} = 0.05$ in Figures 2a, 2b to $t_z/t_{xy} = 0.30$ in Figures 2g–2h. Note the expanded temperature scales on the left panels of Figures 2a–2d. The dense disordered (D), dilute disordered (d), antiferromagnetic (A), and τ phases are shown. The A and τ regions are colored light and dark gray respectively. Second-order phase transitions are drawn with full curves, first-order transitions with dotted curves. The unmarked areas within the dotted curves in the temperature vs. electron density figures are narrow coexistence regions between the two phases at either side. Dashed curves are not phase transitions, but disorder lines between the dense disordered and dilute disordered phases.

between 0.05 and 0.30, while Figure 3 completes the evolution from $t_z/t_{xy} = 0.5$ to the fully isotropic case where $t_z/t_{xy} = 1$. The τ phase is present even for $t_z/t_{xy} = 0.05$ and 0.10, but only at very low temperatures close to the d/D first-order phase transition that itself is distinct by its very narrow coexistence region. As the interplane coupling is increased, the τ phase transition temperatures also get larger, but the density range in which the phase occurs, namely $\langle n_i \rangle$ around 0.65, remains unchanged.

As expected, the antiferromagnetic transition temperatures also increase with the interplane coupling. The phase diagrams all share an antiferromagnetic region near $\langle n_i \rangle = 1$, which is confined to $\langle n_i \rangle$ very close to 1 in

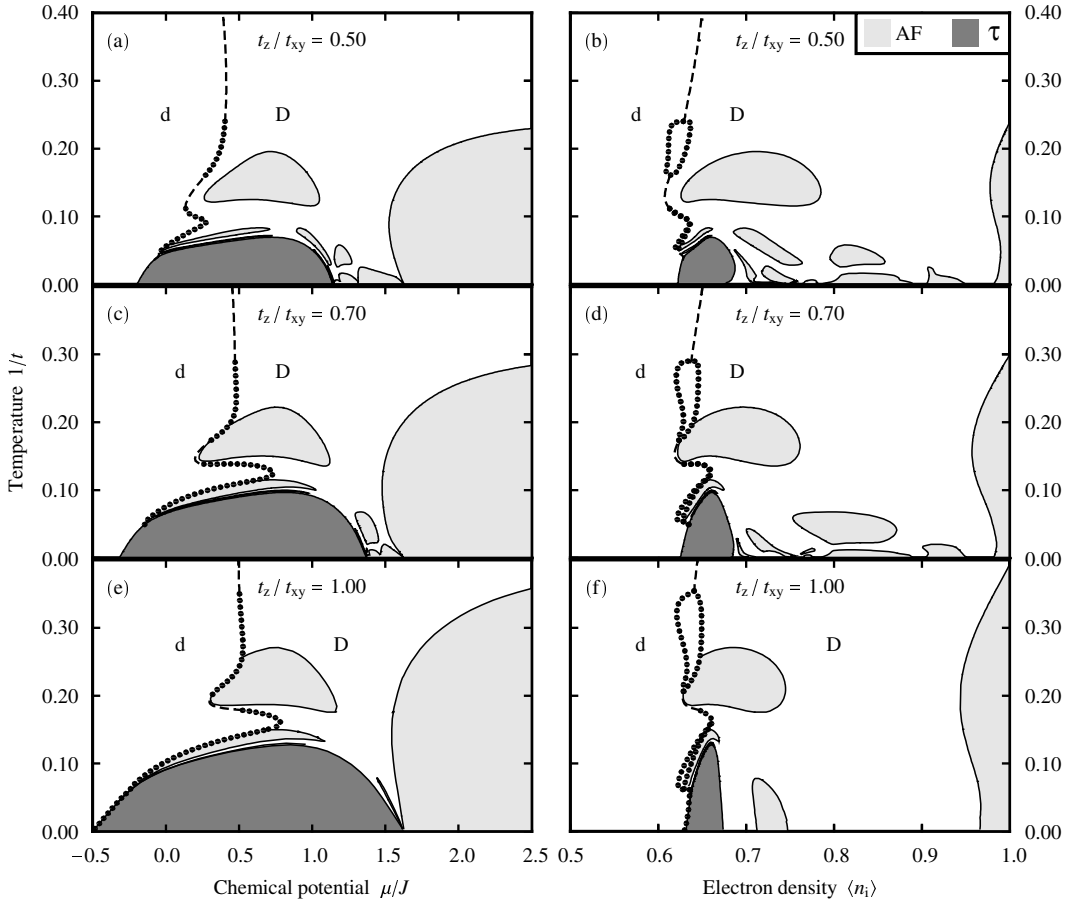

Fig. 3. The continuation of the phase diagrams in Figure 2 for t_z/t_{xy} between 0.5 and 1.

the strongly anisotropic limit, but becomes more stable to hole doping as t_z/t_{xy} gets larger. Away from $\langle n_i \rangle = 1$, in the range of 5–35% hole doping, there are thin slivers and islands of antiferromagnetism separated by regions of the dense disordered phase. For $t_z/t_{xy} = 1$, we see these mostly around the τ phase, but as anisotropy is introduced into the system, the structure of the antiferromagnetic regions becomes more complex, and spread out over a wider range of densities. The lamellar structure of A and D phases here potentially indicates an underlying incommensurate order [9]. The physical significance of this possibility will be discussed below.

Further insight into the nature of the τ phase can be gained by looking at thermodynamic densities on a constant-temperature slice of the phase diagram. Figure 4 plots the chemical potential μ/J, kinetic energy $\langle K \rangle$, and nearest-neighbor spin-spin correlation $\langle \mathbf{S}_i \cdot \mathbf{S}_j \rangle$ at the temperature $1/t = 0.02$ for several values of t_z/t_{xy}. Averages over the xy bonds, $\langle\,\rangle_{xy}$ are drawn with full curves in the figure, and averages taken over the z bonds, $\langle\rangle_z$ are drawn with dashed curves.

Consider first the kinetic energy expectation value $\langle K \rangle = -\sum_\sigma \langle c^\dagger_{i\sigma} c_{j\sigma} + c^\dagger_{j\sigma} c_{i\sigma} \rangle$. The xy bond kinetic energy $\langle K \rangle_{xy}$ grows with hole doping until the density range where the τ phase occurs, and then levels off. This behavior is seen for the whole range of t_z/t_{xy}. We can compare our calculational result here with experimental results in cuprates, by relating the kinetic energy expectation value in the tJ model to the density of free carriers as follows [11]. $\langle K \rangle$ and the total weight of $\sigma_1(\omega, T)$, the real part of the optical conductivity, satisfy the sum rule [24]

$$\int_0^\infty d\omega\, \sigma_1(\omega, T) = \frac{\pi e^2}{2} \langle K \rangle\,. \tag{19}$$

To understand this sum rule, we keep in mind that the tJ Hamiltonian describes a one-band system, so cannot account for interband transitions. For real materials, the full conductivity sum rule has the form

$$\int_0^\infty d\omega\, \sigma_1(\omega, T) = \frac{\pi e^2 n}{2m}\,, \tag{20}$$

where n is the total density of electrons and m is the free electron mass. The right-hand side of equation (20) is independent of electron-electron interactions, in contrast to the right-hand side of equation (19), where $\langle K \rangle$ varies with the interaction strengths in the Hamiltonian. The optical conductivity of actual materials incorporates both transitions within the conduction band and those to higher bands, while the tJ model contains only the conduction band. We can look at equation (19) as a partial sum rule [24,25], which reflects the spectral weight of the free carriers in the conduction band.

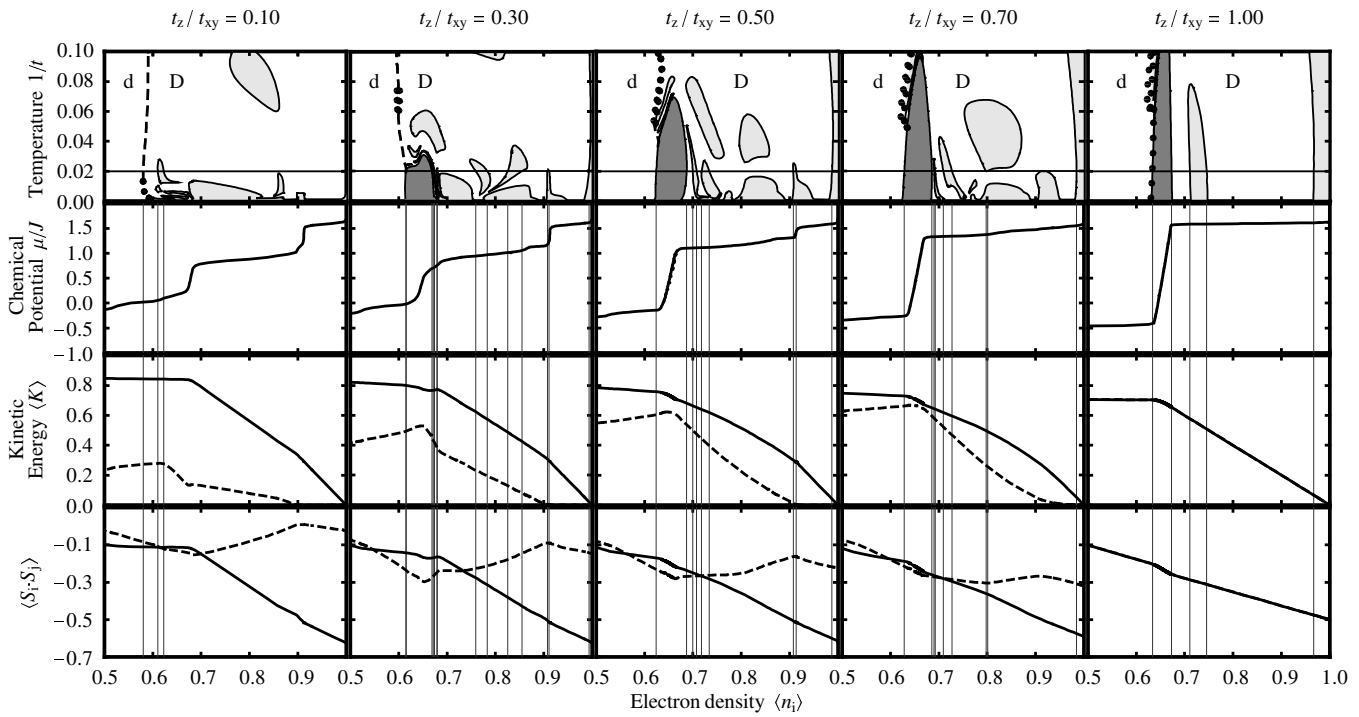

Fig. 4. Thermodynamic properties along slices of the phase diagrams at the constant temperature $1/t = 0.02$. The degree of anisotropy varies from $t_z/t_{xy} = 0.10$ in the first column to $t_z/t_{xy} = 1.00$ in the last column. The top row contains the temperature vs. electron density phase diagrams and a thin horizontal line marking the slice. The antiferromagnetic and τ phases are colored light and dark gray respectively. The rows below this show the chemical potential μ/J, kinetic energy $\langle K \rangle = -\sum_\sigma \langle c^\dagger_{i\sigma} c_{j\sigma} + c^\dagger_{j\sigma} c_{i\sigma} \rangle$, and nearest-neighbor spin-spin correlation $\langle \mathbf{S}_i \cdot \mathbf{S}_j \rangle$. For the $\langle K \rangle$ and $\langle \mathbf{S}_i \cdot \mathbf{S}_j \rangle$ graphs, full curves denote results for nearest neighbors along the xy plane, while dashed curves denote those for nearest neighbors along the z direction. (In the $t_z/t_{xy} = 1$ column, these two curves overlap.) Thin vertical lines mark the location of phase transitions.

The experimental quantity we are interested in is the density of free carriers, which in actual materials is calculated from the low-frequency spectral weight [26],

$$n_{\text{free}}(T) = \frac{2m_b}{\pi e^2} \int_0^{\omega_0} d\omega \, \sigma_1(\omega, T) \,, \tag{21}$$

where m_b is the effective band mass of the electrons. For cuprates, the cut-off frequency is typically chosen around $\hbar\omega_0 \approx 1$ eV so as to include only intraband transitions. In comparison with the tJ model, we identify the right-hand side of equation (19) with

$$\frac{\pi e^2}{2} \langle K \rangle = \frac{\pi e^2 n_{\text{free}}(T)}{2m_b} \,. \tag{22}$$

Puchkov et al. [23] have studied the in-plane optical conductivity of a variety of cuprates, and found that the low-frequency spectral weight increases with doping until the doping level optimal for superconductivity is reached, and then remains approximately constant in the overdoped regime. This behavior of n_{free}/m_b is qualitatively reproduced in our results for $\langle K \rangle_{xy}$.

As for $\langle K \rangle_z$, it is significantly reduced with increasing anisotropy, since interplane hopping is suppressed. $\langle K \rangle_z$ peaks in the τ phase, and decreases for larger dopings. This small peak in $\langle K \rangle_z$, which is most pronounced in the strongly anisotropic regime, is accompanied by an enhancement in the τ phase of the z-bond antiferromagnetic nearest-neighbor spin-spin correlation, $\langle \mathbf{S}_i \cdot \mathbf{S}_j \rangle_z$. For the xy planes, $\langle \mathbf{S}_i \cdot \mathbf{S}_j \rangle_{xy}$ generally increases (i.e., becomes less negative) with hole doping from a large negative value near $\langle n_i \rangle = 1$, as additional holes weaken the antiferromagnetic order. This increase becomes much less pronounced when the τ phase is reached, and $\langle \mathbf{S}_i \cdot \mathbf{S}_j \rangle_{xy}$ becomes nearly constant for large hole dopings in the strongly anisotropic limit. Rather than increasing with hole doping, $\langle \mathbf{S}_i \cdot \mathbf{S}_j \rangle_z$ shows the opposite behavior in the 10–35% doping range, decreasing and reaching a minimum within the τ phase.

The final aspect of the τ phase worth noting is the large change in chemical potential μ/J over the narrow density range where this phase occurs. This is in contrast to broad regions at smaller hole dopings where the chemical potential change is much shallower, and which correspond to those parts of the phase diagram where A and D alternate. We can see this directly in the phase diagram topology in Figures 2 and 3, particularly for larger t_z/t_{xy}. The τ phase has a very wide extent in terms of chemical potential, but becomes very narrow in the corresponding electron density diagram. The converse is true for the

complex lamellar structure of A and D phases sandwiched between the τ phase and the main antiferromagnetic region near $\langle n_i \rangle = 1$. We shall return to this point in our discussion of the purely two-dimensional results.

One can compare our phase diagram results for the tJ model in the strongly anisotropic limit to the large body of work done on the square-lattice tJ model. Here a primary focus has been on the possibility of a superconducting ground-state (or other types of order) away from half-filling, with the presumption that a zero-temperature long-range ordered state in the two-dimensional system would develop a finite transition temperature with the addition of interplanar coupling. Numerical studies using exact diagonalization of finite clusters and variational calculations with trial ground-state wavefunctions have shown enhanced $d_{x^2-y^2}$ pair-pair correlation for $J/t \sim 3$ near $\langle n \rangle = 1/2$ [27,28], and variational approaches have yielded indications of d-wave superconductivity for more realistic parameters like $J/t = 0.4$–0.5 over a range of densities $0.6 < \langle n_i \rangle < 1$ [29–31]. Slave-boson mean-field theory of the tJ model has also predicted a phase diagram with a d-wave superconducting phase within this same doping range away from half-filling [32]. The least biased approach, through high-temperature series expansions, has given mixed signals on this issue. Pryadko et al. [4], using a series through ninth order in inverse temperature, did not observe an increase in the d-wave superconducting susceptibility for the doped system at low temperatures for $J/t < 1$. On the other hand, Koretsune and Ogata [5], using a series up to twelfth order, did see a rapid rise in the correlation length for d-wave pairing with decreasing temperature for densities $0.5 < \langle n_i \rangle < 0.9$, with the largest correlations around $\langle n_i \rangle \sim 0.6$. A similar calculation by Puttika and Luchini [6] also gave a broad, growing peak in the low-temperature d-wave correlation length, but with the maximum shifted to smaller dopings around $\langle n_i \rangle \sim 0.75$. Thus the fact that we see the τ phase emerge near these densities for any non-zero interplanar coupling in the anisotropic tJ model, fits with prevailing evidence for an instability toward d-wave superconductivity away from half-filling in the two-dimensional system.

5 The two-dimensional isotropic tJ model and chemical potential shift

The above analysis leads to a basic question: how do results for a strongly anisotropic $d = 3$ tJ model compare to results obtained directly through a renormalization-group approach for the isotropic $d = 2$ system? The latter was studied in references [8,9], which yielded a phase diagram with only dense and dilute disordered phases, separated by a first-order transition at low temperatures, ending in a critical point, but only for low values of t/J. The absence of any antiferromagnetic order is consistent with the Mermin-Wagner theorem [33]. As seen above, at least a weak coupling in the z direction is required for a finite Néel temperature. What about the absence in $d = 2$ of the τ phase? It turns out that there is a pre-signature of the τ phase in $d = 2$, and it appears exactly where we find the actual phase upon adding the slightest interplane coupling.

In contrast to $d = 3$ even with the weakest coupling between planes, in $d = 2$ the τ phase sink is not a true sink fixed point of the recursion relations, but it is a "quasisink" in the sense that renormalization-group flows come close, stay in its vicinity for many iterations, before crossing over along the disorder line to one of the disordered sinks. We thus find a zero-temperature τ critical point (which emerges from zero temperature with the slightest inclusion of interplanar coupling, leaving behind a true sink). The quasisink behavior is particularly true for trajectories initiating at low temperatures, where the quasisink that is reached is, numerically, essentially indistinguishable from a real one. Since regions of the phase diagram that are approximately basins of attraction of the quasisink are characterized by a sharp rise in the number of iterations required to eventually reach the disordered sinks, we can extract useful information by counting these iterations.

We choose a numerical cutoff for when the interaction constants in the rescaled Hamiltonian have come sufficiently close to their limiting values at any of the high-temperature disordered fixed points (the dilute disordered sink, the dense disordered sink, or the null fixed point in-between). We then count the number of iterations required to meet this cutoff condition for a given initial Hamiltonian. Figure 5 shows the results as contour diagrams, plotted in terms of temperature vs. chemical potential and temperature vs. electron density. There are two clear regions in Figure 5a where the number of iterations blows up at low temperatures. The region for μ/J approximately between –0.5 and 1.6 flows to the τ phase quasisink. When expressed in terms of electron density in Figure 5b, this region is centered around a narrow range of densities near $\langle n_i \rangle = 0.65$, which is where the τ phase actually emerges for finite t_z/t_{xy}. The low-temperature region for $\mu/J \gtrsim 1.6$ flows to an antiferromagnetic quasisink, but does not appear in the electron density contour diagram because the entire region is mapped to $\langle n_i \rangle$ infinitesimally close to 1. This is similar to what we see in the anisotropic model for low t_z/t_{xy}, where the antiferromagnetic region is stable to only very small hole doping away from $\langle n_i \rangle = 1$, but gradually spreads to larger doping values as the interplane coupling is increased. Figure 6 shows the zero-temperature τ fixed point behavior in another way, by plotting the number of renormalization-group iterations as a function of temperature, for two different $\langle n_i \rangle$. For $\langle n_i \rangle = 0.65$, in the τ phase range, the number of iterations diverges as temperature is decreased. In contrast, for $\langle n_i \rangle = 0.75$, not in the τ phase range, the number is nearly constant at all temperatures. In summary, we see that the $d = 2$ results are compatible with the small t_z/t_{xy} limit of the anisotropic model. A weak interplane coupling stabilizes both the τ and antiferromagnetic phases, yielding finite transition temperatures.

We mentioned earlier that the lamellar structure of A and D phases which appears in the anisotropic tJ phase

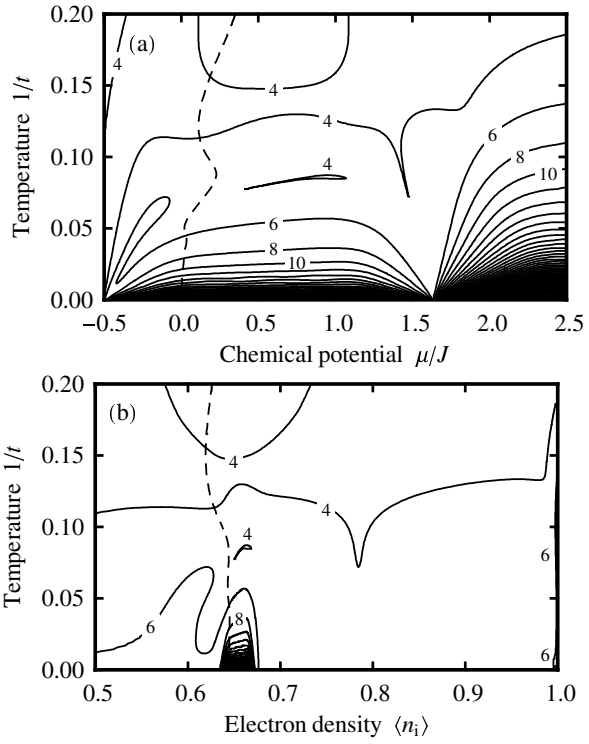

Fig. 5. Contour diagrams showing the number of iterations required to reach a disordered phase sink in the $d = 2$ isotropic tJ model with $J/t = 0.444$. Figure 5a is plotted in terms of temperature vs. chemical potential, while Figure 5b is in terms of temperature vs. electron density. Note the accumulation of contours towards the τ ranges of the chemical potential and density. The disorder line, along which the trajectories eventually cross over from the τ region to disorder, is shown as dashed.

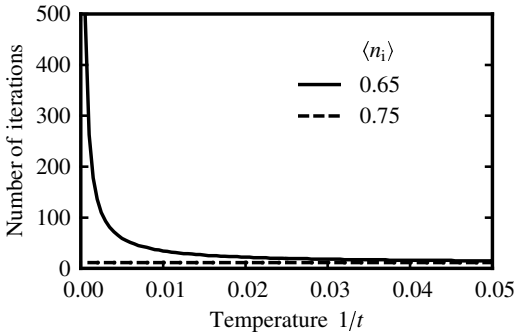

Fig. 6. Number of iterations required to reach a disordered phase sink in the $d = 2$ isotropic tJ model, plotted as a function of temperature for two different values of $\langle n_i \rangle$. The value $\langle n_i \rangle = 0.65$ is in the τ range.

diagram for hole dopings up to the τ phase might be an indicator of incommensurate ordering. One possible form this incommensurate ordering could take is the appearance of stripes, the segregation of the holes into D-like stripes where the hole kinetic energy is minimized, alternating with A-like stripes of antiferromagnetic order. Depending on the arrangement of such stripes with respect to the underlying lattice, the system could flow

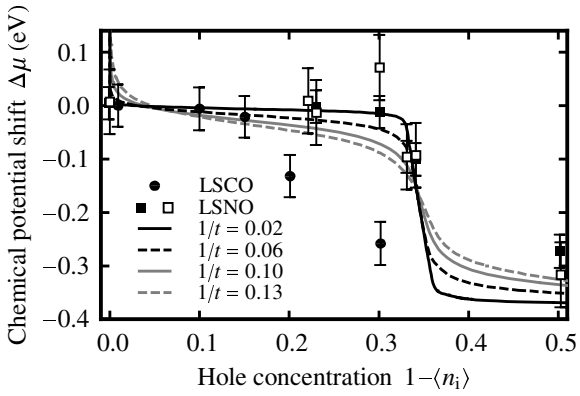

Fig. 7. The calculated chemical potential shift $\Delta\mu$ is plotted as a function of hole concentration $1 - \langle n_i \rangle$ for the isotropic $d = 2$ tJ model, at four different temperatures. For comparison with experimental results, the energy scale $\tilde{t} = 0.1$ eV is chosen. With this scale, the temperatures $1/t = 0.02$, 0.06, 0.10 and 0.13 correspond to 23, 70, 116, and 151 K respectively. Experimental values for $\Delta\mu$ determined from X-ray photoemission spectra at ∼80 K are shown for the cuprate $La_{2-x}Sr_xCuO_4$ (LSCO, filled circles) [34] and the nickelate $La_{2-x}Sr_xNiO_4$ (LSNO, filled squares) [35]. For LSNO we also show another experimental estimate based on ultraviolet photoemission spectra (open squares), taken at 150 K, except for the datapoint at zero hole concentration, which was taken at 230 K [35].

under repeated renormalization-group transformations either to the antiferromagnetic or dense disordered sink. Since the arrangement of the stripes will vary as we change the temperature or density in the system, this could lead to a lamellar structure of A and D phases in the resulting phase diagram. Though we cannot probe the existence of such stripes directly in our approach, an observable consequence of stripe formation would be the suppression of the chemical potential shift when additional holes are added to the system, since we effectively have a phase separation on a microscopic scale into hole-rich and hole-poor regions. Indeed, inquiries into stripe formation in experimental systems doped away from half-filling often look for this tell-tale pinning of the chemical potential. For example, in the cuprate superconductor $La_{2-x}Sr_xCuO_4$ (LSCO), photoemission measurements of core levels have shown that the chemical potential shifts by a small amount (<0.2 eV/hole) in the underdoped region, $\delta \equiv 1 - \langle n_i \rangle \lesssim 0.15$, compared to a large shift (∼1.5 eV/hole) in the overdoped region, $\delta \gtrsim 0.15$, an observation which has been interpreted as a possible signature of stripes [34]. In non-superconducting systems where the existence of stripes is clearly established, like the nickelate $La_{2-x}Sr_xNiO_4$ (LSNO), we see a qualitatively similar behavior, with the chemical potential shifting significantly only for high-doping ($\delta \gtrsim 0.33$ for LSNO) [35]. For the tJ model, we take the chemical potential shift as $\Delta\mu = \tilde{\mu} - \tilde{\mu}_0$, where $\tilde{\mu}_0$ is the chemical potential below which $\langle n_i \rangle$ begins to the decrease noticeably from 1 in the low temperature limit. Figure 7 shows our calculated $\Delta\mu$ vs. hole concentration for the $d = 2$ tJ model at four different temperatures.

In order to compare with the experimental data for LSCO and LSNO, we choose an energy scale $\tilde{t} = 0.1$ eV. For the low-doping region, where interplane coupling generates a lamellar structure of A and D phases, the slope of the $\Delta\mu$ curve remains small. On the other hand, for high-doping, in the range of densities corresponding to the τ phase, $\Delta\mu$ turns steeply downward. The similarities between this behavior and the experimental data supports the idea of stripe formation in the low-doping region.

This research was supported by the US Department of Energy under Grant No. DE-FG02-92ER-45473, by the Scientific and Technical Research Council of Turkey (TÜBITAK), and by the Academy of Sciences of Turkey. MH gratefully acknowledges the hospitality of the Feza Gürsey Research Institute and of the Physics Department of Istanbul Technical University.

References

1. E. Dagotto, Rev. Mod. Phys. **66**, 763 (1994)
2. M. Imada, A. Fujimori, Y. Tokura, Rev. Mod. Phys. **70**, 1039 (1998)
3. S. Chakravarty, H.-Y. Kee, K. Völker, Nature **428**, 53 (2004)
4. L.P. Pryadko, S.A. Kivelson, O. Zachar, Phys. Rev. Lett. **92**, 067002 (2004)
5. T. Koretsune, M. Ogata, J. Phys. Soc. Jpn **74**, 1390 (2005)
6. W.O. Putikka, M.U. Luchini, e-print `arXiv:cond-mat/0507430`
7. G. Su, Phys. Rev. B **72**, 092510 (2005)
8. A. Falicov, A.N. Berker, Phys. Rev. B **51**, 12458 (1995)
9. A. Falicov, A.N. Berker, Turk. J. Phys. **19**, 127 (1995)
10. M. Hinczewski, A.N. Berker, Eur. Phys. J. B **48**, 1 (2005)
11. M. Hinczewski, A.N. Berker, e-print `arXiv:cond-mat/0503631`
12. A. Erbaş, A. Tuncer, B. Yücesoy, A.N. Berker, Phys. Rev. E **72**, 026129 (2005)
13. A.A. Migdal, Zh. Eksp. Teor. Fiz. **69**, 1457 (1975) [Sov. Phys. JETP **42**, 743 (1976)]
14. L.P. Kadanoff, Ann. Phys. (N.Y.) **100**, 359 (1976)
15. A.N. Berker, S. Ostlund, J. Phys. C **12**, 4961 (1979)
16. R.B. Griffiths, M. Kaufman, Phys. Rev. B **26**, 5022 (1982)
17. M. Kaufman, R.B. Griffiths, Phys. Rev. B **30**, 244 (1984)
18. M. Suzuki, H. Takano, Phys. Lett. A **69**, 426 (1979)
19. H. Takano, M. Suzuki, J. Stat. Phys. **26**, 635 (1981)
20. A.N. Berker, S. Ostlund, F.A. Putnam, Phys. Rev. B **17**, 3650 (1978)
21. R. Shankar, V.A. Singh, Phys. Rev. B **43**, 5616 (1991)
22. C. Bernhard, J.L. Tallon, T. Blasius, A. Golnik, C. Niedermayer, Phys. Rev. Lett. **86**, 1614 (2001)
23. A.V. Puchkov, P. Fournier, T. Timusk, N.N. Kolesnikov, Phys. Rev. Lett. **77**, 1853 (1996)
24. L. Tan, J. Callaway, Phys. Rev. B **46**, 5499 (1992)
25. D. Baeriswyl, C. Gros, T.M. Rice, Phys. Rev. B **35**, 8391 (1987)
26. J. Orenstein, G.A. Thomas, A.J. Millis, S.L. Cooper, D.H. Rapkine, T. Timusk, L.F. Schneemeyer, J.V. Waszczak, Phys. Rev. B **42**, 6342 (1990)
27. E. Dagotto, J. Riera, Phys. Rev. Lett. **70**, 682 (1993)
28. E. Dagotto, J. Riera, Y.C. Chen, F. Alcaraz, F. Ortolani, Phys. Rev. B **49**, 3548 (1994)
29. M. Kohno, Phys. Rev. B **55**, 1435 (1997)
30. H. Yokoyama, M. Ogata, J. Phys. Soc. Jpn **65**, 3615 (1996)
31. S. Sorella, G.B. Martins, F. Becca, C. Gazza, L. Capriotti, A. Parola, E. Dagotto, Phys. Rev. Lett. **88**, 117002 (2002)
32. P.A. Lee, N. Nagaosa, X.-G. Wen, Rev. Mod. Phys. **78**, 17 (2006)
33. N.D. Mermin, H. Wagner, Phys. Rev. Lett. **17**, 1133 (1966)
34. A. Ino, T. Mizokawa, A. Fujimori, K. Tamasaku, H. Eisaki, S. Uchida, T. Kimura, T. Sasagawa, K. Kishio, Phys. Rev. Lett. **79**, 2101 (1997)
35. M. Satake, K. Kobayashi, T. Mizokawa, A. Fujimori, T. Tanabe, T. Katsufuji, Y. Tokura, Phys. Rev. B **61**, 15515 (2000)